W-Band Switch-Less Reconfigurable-Push Dual-Band VCO Using Clover-Shaped Inductor and Robust Triple Cores for 6G Communications

Seongwoog Oh, *Graduate Student Member, IEEE*, Jinhyun Kim, *Graduate Student Member, IEEE*, and Jungsuek Oh, *Senior Member, IEEE*

***Abstract*— This study proposes a switchless reconfigurable triple-push/push–push dual-band voltage-controlled oscillator (VCO) topology to design a *W*-band metal–oxide–semiconductor (CMOS) for 6G communications. The proposed clover-shaped inductor consists of three branch inductors, where each node had a symmetrical layout, connecting to each another and to the output pad. This topology was demonstrated in a *W*-band VCO using three cross-coupled cores with an ON/OFF-state control to achieve triple-push and push–push operations. An oscillating core based on a robust cross-coupled structure avoids the oscillation startup issue, while achieving a 120° phase offset through a vector-sum-based method. The measured center frequencies of the bands were 91.04 and 102.33 GHz, with the tuning ranges of 10.4% and 14.1%, respectively. The proposed VCO with an independent core ON/OFF-state control enables a low parasitic switchless frequency band shift, resulting in a superior tuning range compared with those of conventional dual-/single-band VCOs. The effectiveness of this approach was demonstrated through fabrication in a 28-nm CMOS process, with a best FOM$_T$ value of −178.6 dBc/Hz for the full band.**

***Index Terms*— Current distribution, dual band, push–push technique, reconfigurable oscillation, triple-push technique, voltage-controlled oscillator (VCO).**

I. Introduction

6G MOBILE communication, which will be commercialized within the next decade, requires higher data rates and lower latency than 5G [1]. To satisfy these requirements, sub-terahertz (sub-THz) bands with the frequencies of 90–300 GHz are being actively studied as candidates for the carrier frequency. The *W*-band has been widely studied as a passive/active imaging application over the past few decades [2], [3]. In addition, it has broadband and low-interference characteristics, making it suitable for sub-THz communication [4]. In both mobile communication and radar systems, an integrated voltage-controlled oscillator (VCO) is one of the most critical RF blocks. Broadband sub-THz VCO designs have various issues that must be addressed, such as low Q-factor values of resonant tanks, limited transistor capability to generate negative transconductance (G_m), and narrow frequency tuning ranges (FTRs).

Manuscript received 16 September 2022; revised 11 December 2022 and 27 January 2023; accepted 13 February 2023. This work was supported in part by the Institute of Information and Communications Technology Planning and Evaluation (IITP) through the Korea Government (MSIT) under Grant 2021-0-00763, in part by Innovative Fusion Technologies (Intelligent Antenna Material/Structure/Network for THz 6G) (50%), and in part by Samsung Electronics (Development of Dualband/Wide-band High Efficiency Power Amplifier Monolithic Microwave Integrated Circuit (MMIC) for 5G Applications) (50%). This paper is an expanded version from the 2022 IEEE RFIC Symposium, Denver, CO, USA, June 19—21, 2022. *(Corresponding author: Jungsuek Oh.)*

The authors are with the Department of Electrical and Computer Engineering (ECE), Institute of New Media and Communications (INMC), Seoul National University, Seoul 151-742, Republic of Korea (e-mail: jungsuek@snu.ac.kr).

Color versions of one or more figures in this article are available at https://doi.org/10.1109/TMTT.2023.3253545.

Digital Object Identifier 10.1109/TMTT.2023.3253545

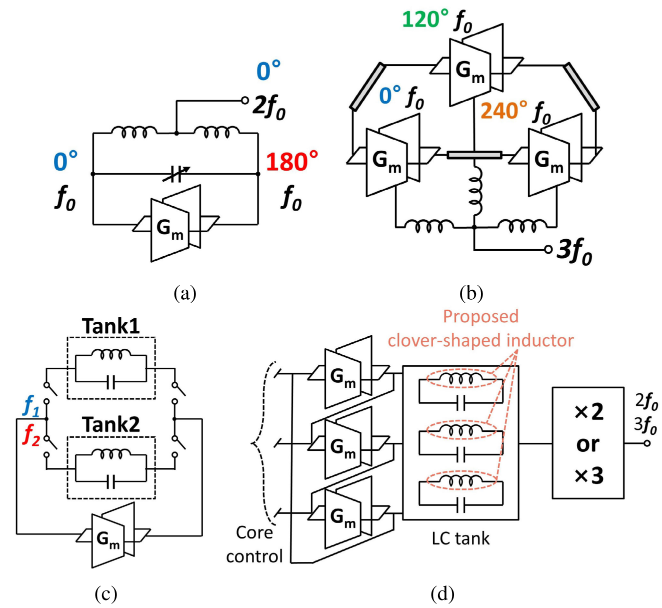

Fig. 1. Simplified schematic of implementing conventional (a) push–push, (b) triple-push, and (c) dual-band VCOs, and (d) proposed switch-less reconfigurable-push dual-band VCO.

VCOs using push–push or triple-push oscillation techniques have been extensively studied at the millimeter wave range and above to solve fundamental oscillation startup issues owing to the low Q-factor of the resonance tank and small negative impedance generated by the active core, as shown in Fig. 1(a) and (b). Previous studies regarding push–push VCOs attempted to overcome the mentioned problems using transmission-line-based standing wave, varactor-less, and G_m-boosting techniques [5], [6], [7]. A transmission line-based oscillation topology has the advantage of a low phase noise based on a high Q-factor tank compared with an LC configuration. However, because many G_m cells are required, high dc power consumption and narrow FTR are inevitable problems. A varactor-less oscillation structure can achieve the most elevated tank Q-factor; however, this is impractical, because the oscillation frequency fluctuating due to the parasitic capacitance of the transistor constituting the oscillation core is highly sensitive to bias voltage changes. The varactor-less technique also has a narrow FTR, because the rate of change of the parasitic capacitance with the tuning voltage is below 10%. The G_m-boosting technique can achieve a high output power while solving the VCO startup issue. However, the FTR becomes narrow, because the large-sized transistors are added to the oscillation node for sufficient G_m. Studies regarding triple push have been conducted by combining six inductive elements based on ring oscillator cores [8], [9], [10]. Six inductive elements based on three cores can achieve a high fundamental and second-harmonic suppression. However, six inductors require a large area, in addition to causing asymmetries in the layout, thus increasing the power of the unwanted harmonics or degrading the Q-factor of the oscillation tank at the target frequency.

Switching between multiple resonant tanks that resonate at different target frequencies is the most popular technique for implementing the dual band, as shown in Fig. 1(c). Owing to the performance degradation caused by the ON-resistance of the switch, recent studies regarding dual-band oscillators have modified the resonant tank, adjusting the current coupling and connecting the switch to the ground shield to minimize the effect of the switch resistance [11], [12], [13]. However, because the RF current flows through the switch-on resistor in all cases, the Q-factor is inevitably degraded by the switch resistor, which results in a lower performance than that of the single-band oscillator.

As shown in Fig. 1(d), a three-core configuration based on a cross-coupled topology combined with a clover-shaped inductor is proposed to achieve dual-band resonance in the W-band and to achieve reconfigurable push–push and triple-push oscillations. A clover-shaped inductor is laid out for combining with three cores and simultaneously has three symmetrical branch inductors. Each core is turned off and activated to generate a push–push or triple-push signal from the same output node, enabling a switchless dual-band operation.

Fig. 1(d) shows a simplified block diagram of the VCO proposed in this study. Among the resonant tank and active core of VCO, a triple cross-coupled core configuration and a clover-shaped inductor are proposed for dual-band reconfigurable oscillation. The oscillation startup issue is avoided through push–push or triple-push techniques rather than a fundamental resonance, and simultaneously, a practical FTR is obtained by the proposed inductor with the varactors. This study is an extended version of our previous study [14], which was the first demonstration of a CMOS VCO designed using the proposed clover-shaped inductor. Section II presents the principle of operation of the clover-shaped inductor and the design methodology through circuit analysis, and Section III describes the design of active cores for using optimized inductors. Finally, the fabrication and measurement results of the optimized VCO are covered in Section IV.

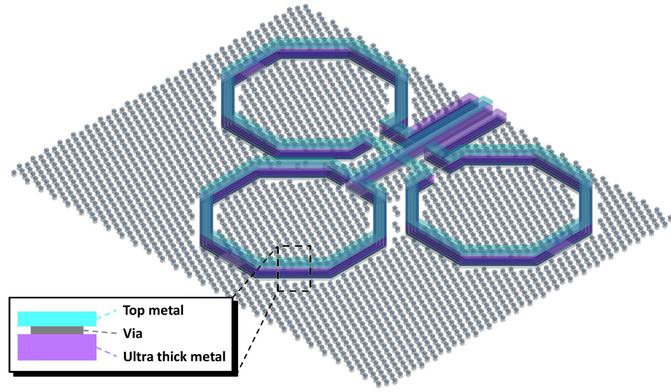

Fig. 2. Proposed clover-shaped inductor with three branch inductors.

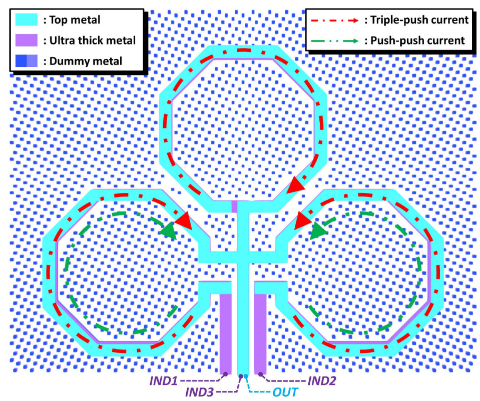

Fig. 3. Triple-push/push–push mode current path of clover-shaped inductor.

II. Design of a Clover-Shaped Inductor

A. Operation of Reconfigurable Push

The overall structure of the proposed clover-shaped inductor is illustrated in Fig. 2. Three single-loop inductor branches with two metal layers (top and ultra-thick metal) are arranged in a clover shape. As shown in Fig. 3, one end of each branch is connected using a top metal, which is the output of the oscillator. The nodes that are not connected to the other branches were configured as IND1, IND2, and IND3. When a signal excites all the inductor branch nodes, the current follows a triple-push current path. If only IND1 and IND2 are excited while IND3 remains in series with the off parasitic capacitor, the series LC impedance can cause an unexpected leakage in the push–push current path. Fig. 4(a) demonstrates the potential of each frequency harmonic with respect to the excitation and with a phase difference of 120° to each branch inductor node for the triple-push operation. Only the third-harmonic signal is emitted from the output node, whereas both the fundamental and second-harmonic frequencies are canceled. Considering the configuration with the oscillation core, a parasitic capacitance of the varactor and transistor is present despite the lack of signal excitation at the IND3 node. Thus, there appears to be an equivalent series inductor–capacitor loading at the output node, which can degrade the output power in the second-harmonic band.

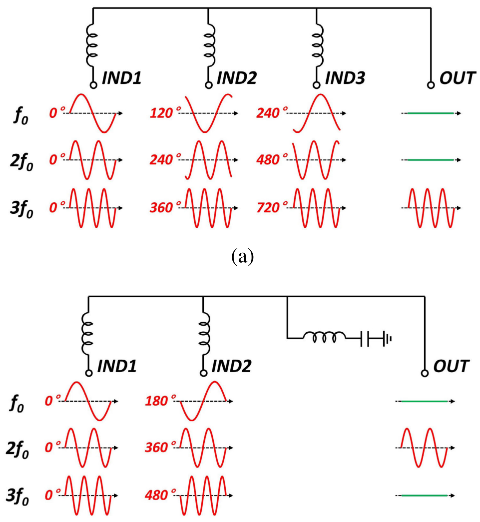

Fig. 4. Signals generated at the output node according to the excitation and phase of each node for (a) triple-push and (b) push–push operations.

Fig. 4(b) demonstrates a differential signal being excited to only two nodes, and a second-harmonic signal is extracted from the output. By utilizing the 0°/180°/open or 0°/120°/240° phase of the proposed clover inductor, the reconfigurable-push operation can be achieved at the same output node.

B. Analysis of Unused Branch Inductor Effect

The proposed clover-shaped inductor performs the triple-push operation in accordance with well-known principles [15]. However, in the push–push mode, there is an additional branch inductor that is not used in the current path; therefore, a design method that considers this must be utilized. Fig. 5(a) demonstrates a detailed push–push equivalent circuit for checking the effect of the unused branch. An oscillating core located between nodes IND1 and IND2 produces a differential signal that is delivered to the output node between the two branch inductors. The IND3 branch and varactor in series are denoted as L_{branch} and C_{cent}, respectively. The simulated transmission coefficient between the center and output node with a parallel loaded Z_{cent} according to the voltage tuning of the varactor is shown in Fig. 5(b). A −35-dB notch response is demonstrated at a fundamental oscillation frequency of 45 GHz, confirming that it assists in suppressing the fundamentals of the push–push operations. At the target second-harmonic frequency of the 90-GHz band, it generates a loss of 5.6 ± 0.85 dB due to leakages. In addition, the loaded Z_{cent} affects the branch inductor characteristics at the fundamental frequency. As shown in Fig. 5(c), the calculated differential characteristics of the branch inductor are affected by C_{cent}. The characteristics of the differential mode were calculated using the conversion formula from the two ports to the differential one port [16] by connecting the ports to the IND1 and IND2 nodes

$$L_{\text{diff}} = \frac{\text{imag}(Z_{11} - Z_{12} - Z_{21} + Z_{22})}{2\pi f_0} \tag{1}$$

$$Q_{\text{diff}} = \frac{\text{imag}(Z_{11} - Z_{12} - Z_{21} + Z_{22})}{\text{real}(Z_{11} - Z_{12} - Z_{21} + Z_{22})}. \tag{2}$$

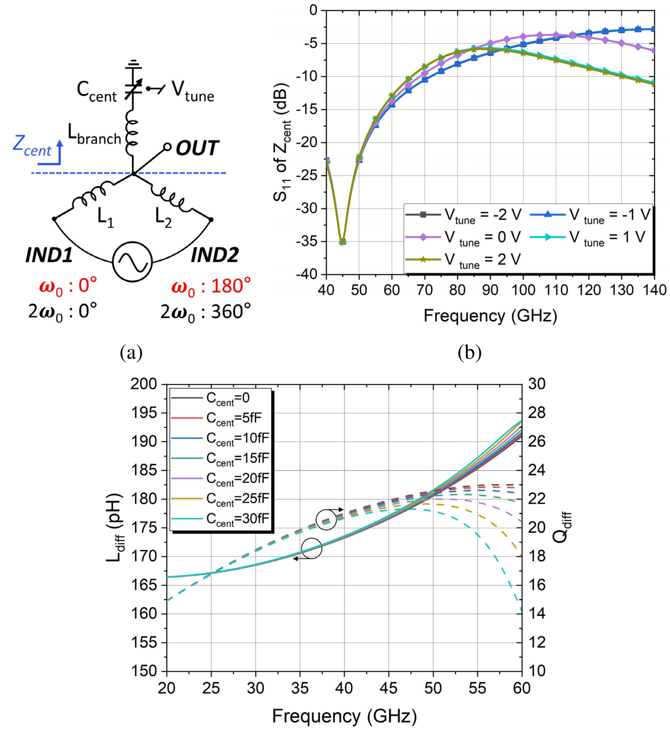

Fig. 5. (a) Equivalent circuit of the proposed clover-shaped inductor under a push–push operation. Simulated (b) transmission frequency response of Z_{cent} and (c) differential-mode inductance/Q-factor of a branch inductor.

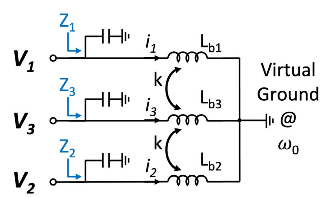

Fig. 6. Schematic of the proposed clover-shaped inductor under triple-push operation with nonuniform couplings.

Although the characteristic change can be neglected in the low-frequency band (<42.5 GHz), the Q-factor of the inductor is too low for the oscillation tank. In the high-frequency band (>47.5 GHz), the Q-factor is reduced by 39% at 60 GHz owing to the C_{cent} changes from 0 to 30 fF. Therefore, 45 GHz is selected as the VCO target fundamental frequency due to the difference in the Q-factor, with the maximum being only one, and the C_{cent} degradation effect remains within 5%.

C. Analysis of the Effect of Nonuniform Coupling Between Branches

As shown in Fig. 6, when a signal is excited to all the branches of the proposed inductor, nonuniform coupling between the branches must be considered. Because the mutual coupling experienced between the center branch and branches located at both ends is different, the design must be ensure that the resonant frequency at each node exhibits the same value. For simplicity, the coupling between the V_1 and V_2 node inductors is ignored from the equivalent circuit analysis due to the branch location having a coupling coefficient of 0.01 or less [17]. As shown in Fig. 2, when considering a symmetrical layout, the assumptions $V_1 = V_2$ and $i_1 = i_2$ can be applied. Therefore, the voltage at each node can be expressed as follows:

$$\begin{aligned} V_1 &= V_2 = i_1 Z_1(\omega_{\mathrm{osc1}}) + i_3 e^{j\theta} k L_{b3} \\ V_3 &= i_3 Z_3(\omega_{\mathrm{osc2}}) + 2\, i_1 \cos(\theta) k L_{b1}. \end{aligned} \tag{3}$$

Here, Z denotes the impedance, including the parallel capacitance and resistance corresponding to the resonance at each node, ω denotes the resonance frequency of each node, θ denotes the phase difference between the nodes ($\theta = 2\pi/3$ for triple push), k denotes the coupling coefficient between the two branches, and L_b is the self-inductance of each branch. The impedance of the resonant tank is expressed as follows:

$$Z_1(\omega) = \frac{R}{1 + j\frac{2Q}{\omega_0}(\omega - \omega_0)} \tag{4}$$

where Q denotes the Q-factor of the tank, and w_0 denotes the resonant frequency of the LC directly loaded into the tank. The resonant frequency of each node can be derived by combining (3) and (4)

$$\begin{aligned} \omega_{\mathrm{osc1}} &\approx \omega_{01} - \frac{\omega_{01}}{2Q}\frac{\sqrt{3}nkL_{b3}}{2R} \\ \omega_{\mathrm{osc2}} &= \omega_{02} = \frac{1}{\sqrt{L_{b3}C_{\mathrm{tank}}}} \end{aligned} \tag{5}$$

where n denotes the current ratio of i_3/i_1. The center branch suffers from multiple couplings through the mutual inductance of the two branches, but only the real part of the impedance is affected owing to the cancellation of the imaginary parts of the signals with $+120°$ and $-120°$ offset phases. Therefore, ω_2 exhibits a resonance frequency that is independent of coupling. For a practical triple-push operation, each node must have the same achievable resonant frequency ($\omega_{\mathrm{osc1}} = \omega_{\mathrm{osc2}}$). The conditions for the required coupling coefficient based on these conditions are as follows:

$$k \ll \frac{2QR}{\sqrt{3}nL_{b3}}. \tag{6}$$

Because the molecular term in (6) represents only the reactance of the tank, it can be optimized independent of the inductor design without compromising the phase noise performance. Typically, n converges to one in steady state, and L_{b2} indicates a pH inductance ranging from tens to hundreds; thus, it is possible to design a clover-shaped inductor with k suitable for avoiding nonuniform coupling effects.

III. Switch-Less Dual-Band VCO Implementation

A. Robustness of the Oscillation Core

The Colpitts, ring, and cross-coupled topologies are used as an oscillation core to implement several W-band or higher VCOs. The robustness of each oscillation core topology is simulated with a negative G_m (Y_{core}) to select an appropriate topology that avoids the oscillation startup problem. Fig. 7 demonstrates the Y-parameters' real part for the oscillation tank and G_m for each oscillation core topology composed of NMOS transistors based on the bulk CMOS process. For the same dc power dissipation, only the cross-coupled structure resulted in an absolute tank-G_m ratio (=real(Y_{core})/real(Y_{tank})) of greater than 1.5. The cross-coupled design has the advantage of consuming one less voltage headroom compared with the Colpitts and ring structure. At the resonance frequency, the cross-coupled core gain of the loop must satisfy the following condition:

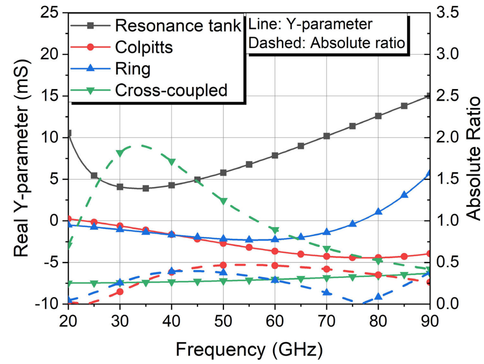

Fig. 7. Y-parameters' real part and tank-G_m ratio of each oscillating core topology and oscillation core.

$$|A_v| = |-g_m R_p| > 1 \tag{7}$$

where R_p denotes the equivalent parasitic resistances at the resonance frequency ($\omega = 1/(L_{\mathrm{eq}}C_{\mathrm{eq}})^{1/2}$) for stable oscillation [18]. Assuming that an appropriate phase offset is provided, the cross-coupled and ring topologies demonstrate the most relaxed conditions through (7) for each oscillating core gain. Ring-based cores can achieve a greater loop gain; however, the requirements of an additional 120° phase offset loading and difficulties in creating a differential signal make them less attractive. Therefore, a core with a cross-coupled structure at a frequency above the millimeter wave, where it is difficult to achieve an enhanced g_m, should be used.

B. Proposed VCO Design

Fig. 8 presents a schematic illustration of the proposed W-band switchless reconfigurable dual-band VCO. Each core was based on a cross-coupled structure composed of 24-μm M_N pairs to generate a negative transconductance with capacitive feedback to independently apply the gate voltage for on/off control. V_{dd} was applied to the output node of a clover-shaped inductor through a bias-T circuit, in which a tripled or doubled signal is formed. The LC tank consisted of a clover-shaped inductor, and three varactors connected to a dc block were loaded on each inductor port. The diameter and metal width of each branch of the optimized clover-shaped inductor were 60 and 6 μm, respectively. If a pair of varactors is connected between each port as a typical cross-coupled VCO, a virtual ground is not guaranteed in the middle of the pair for the triple-push operation. The length and width sizes of the used varactors were 0.5 and 10 μm, respectively. Thus, a current path was formed through the varactors from one port to another, creating an additional unintended resistance

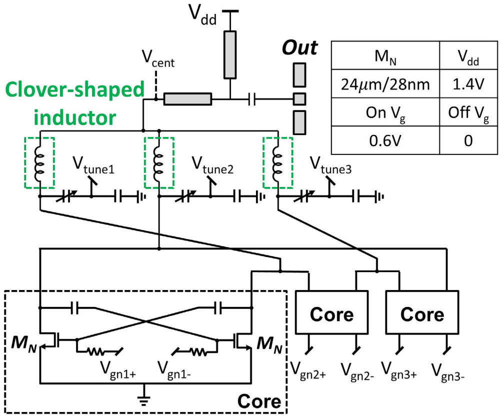

Fig. 8. Schematic of the *W*-band switch-less reconfigurable dual-band VCO consisting of three cores and a clover-shaped inductor.

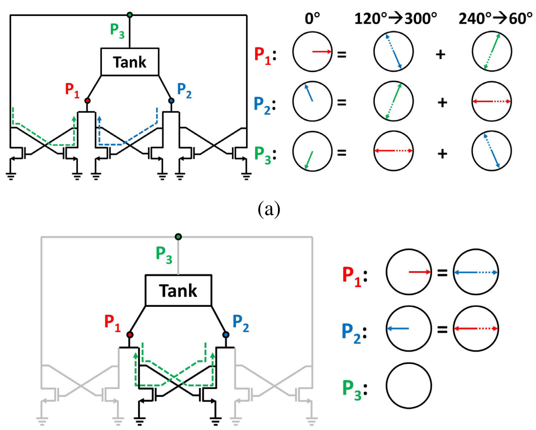

(a)

(b)

Fig. 9. Operation phase diagram of the proposed VCO topology at the fundamental frequency for (a) triple-push and (b) push–push modes.

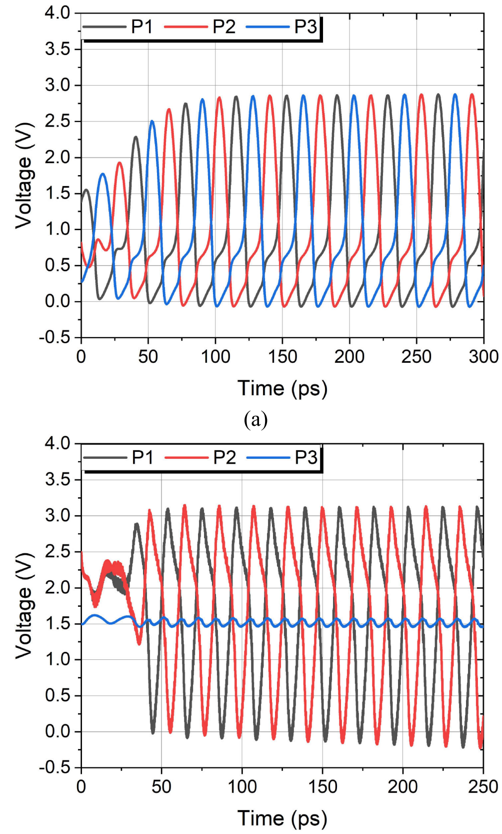

(a)

(b)

Fig. 10. Oscillation startup voltage waveform of the proposed VCO at each node for (a) triple-push and (b) push–push modes.

component. The reconfigurable dual-band oscillation of the VCO was controlled by the gate voltage applied to each core. The triple-push operation was configured when 0.6 V was applied to the gates of all cores. For the push–push operation, V_{gn1} was 0.6 V, and no voltage was applied to the remaining cores to ensure that the cores remained off. Because no switch was connected to the VCO oscillation node, the possibility of parasitic capacitance is minimized. Therefore, the proposed dual-band VCO is capable of a frequency-tuning range performance comparable to that of the single-band topology.

The oscillation principle of the proposed VCO at the fundamental resonant frequency is shown in Fig. 9. $P1$, $P2$, and $P3$ indicate the nodes connected to the tank with two connected drains. For the triple-push mode, the signal of $P1$ is a result of the adding $P2$ and $P3$ through each core. The dotted line indicates the phase of the signals of the other two nodes, and the solid line is the 180° inverted phase for the vector sum. The phases of each signal from $P2$ and $P3$ undergo a 180° phase shift through the core. By repeating the aforementioned procedure, the vector sum of $P2$ having a phase of 120° and $P3$ having a phase of 240° forms a $P1$ signal of 0°. The $P2$ and $P3$ signals were also formed through the same principle as $P1$. The closed-loop gain becomes unity at the resonant frequency, because the negative conductance compensates for the parallel resistance of the tank according to Barkhausen's criteria. Therefore, each core exhibits a 180° phase shift and vector-summed amplitude gain of unity as a typical differential oscillator on each cross-coupled core, thus resolving the limitation of a 180° difference between the differential nodes of the cross-coupled core by introducing a tri-core with drain sharing between the two cores. As shown in Fig. 9(b), in the push–push mode, the proposed VCO operates in the same manner as the conventional push–push VCOs based on fundamental differential signals.

The oscillation startup voltage waveform for each node was plotted according to each operation to verify the analysis of the VCO phase diagram via simulations. As shown in Fig. 10(a), the phase of node $P2$ follows node $P3$ at 5 ps and node $P1$ at 16 ps. First, the vector sum converges through the feedback, which is followed by the voltage magnitude level falling into the steady state. Fig. 10(b) demonstrates the voltage waveform up to the steady state during the push–push operation. Unlike the triple-push operation, if the loop gain is reduced by the vector sum of a 120° phase difference, a push–push operation that generates a 180° phase difference based on a cross-coupled core can reach the steady state faster, such as from 100 to 44 ps. Because a virtual ground is formed at the fundamental frequency at the center output node, the frequency of the voltage formed at the $P3$ node only has the

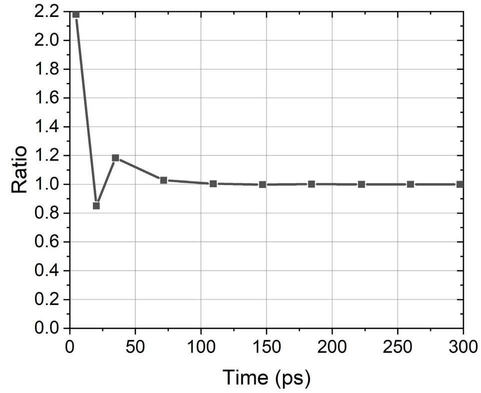

Fig. 11. Ratio (n) of voltages between $P1$ and $P2$ nodes that converge with time.

second harmonic. As depicted in Section II-B, a voltage swing of 0.11 V_{pp} is achieved by utilizing the design methodology to minimize the power leakage at the second harmonic by unused branches. Furthermore, the current ratio n, which was included in the conditions of the coupling coefficients (k) that are analyzed in Section II-C, was verified by simulation. Considering the symmetry of each core and branch inductor constituting the VCO, the current ratio can be converted to the ratio of the voltage swing as follows:

$$n = \frac{i_3}{i_1} = \frac{i_3 Z_{\text{tank}}}{i_1 Z_{\text{tank}}} = \frac{V_3}{V_1} \tag{8}$$

where Z_{tank} denotes the tank impedance at the resonant frequency. As shown in Fig. 11, n fluctuates before 100 ps and converges to 1 over time, confirming that the convergence condition assumed in the previous analysis was valid.

Because the proposed dual-band VCO operates based on reconfigurable push, the design should be optimized to obtain the maximum harmonic power at the output node. Fig. 12(a) illustrates the voltage waveforms generated at each node; the output node of the oscillation core during the triple-push operation. The voltage at node $P1$ exhibiting a rail-to-rail voltage swing presents an asymmetrical waveform; therefore, it can be expressed as an equation containing harmonics as follows:

$$V_{\text{eqn1}} = a_0 + a_1 \sin(\omega_0 t + \theta_1) + a_2 \sin(2\omega_0 t + \theta_2) + a_3 \sin(3\omega_0 t + \theta_3) \tag{9}$$

where subscript a denotes the amplitude of each harmonic including dc, ω_0 denotes the resonant frequency, and θ denotes the phase offset value of each harmonic. The equation sufficiently agrees with the simulated waveform when the ratio of the third harmonic of the design target to the fundamental signal, a_3/a_1, is 0.14, and a_2/a_1 is 0.54. Similarly, $P2$ and $P3$ are the $P1$ signal added by a 120° phase offset. In the case of the output node voltage, V_{cent}, a_1, and a_2 of the resonance tank node signals are canceled, and only the a_3 component exists; thus, it can be expressed as a single sine wave as follows:

$$V_{\text{eqn2}} = a_0' + a_3' \sin\left(3\omega_0 t + \theta_3'\right) \tag{10}$$

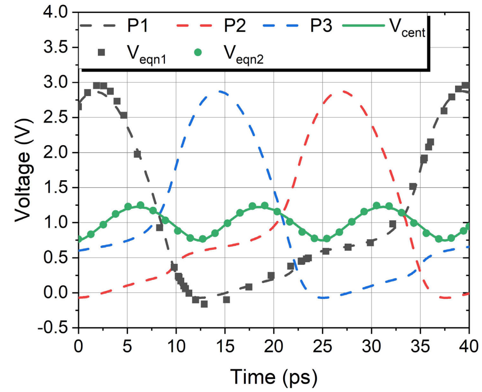

(a)

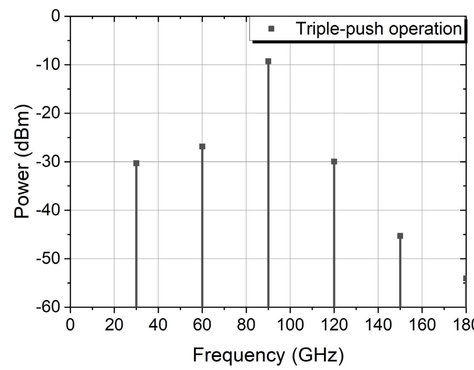

(b)

Fig. 12. Comparison of the fundamental and third-harmonic signal (a) voltage waveforms and (b) frequency spectrum of the proposed VCO in the triple-push mode.

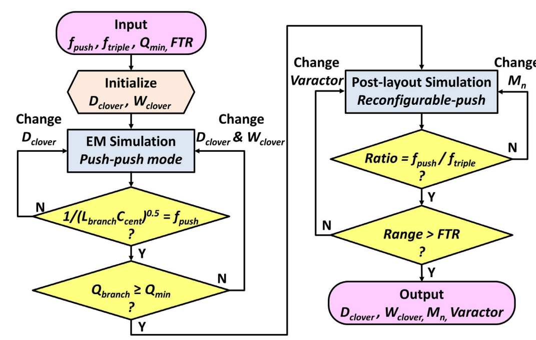

Fig. 13. Design flow for implementing VCO utilizing the proposed clover-shaped inductor and oscillation core configuration.

with a_3' equal to 0.24. Fig. 12(b) shows that the fundamental and second-harmonic powers can be suppressed by 21 and 17.6 dB, respectively.

Fig. 13 summarizes the design flows for implementing the VCO presented in this study. To design the VCO, the target frequency band (f_{push} and f_{triple}), minimum Q-factor ($Q_{\min}$), and FTR are set. First, the diameter of each branch (D_{branch}) that makes up the clover-shaped inductor and the width of the metal winding (W_{branch}) should be initialized. To prevent the leakage to the off cores in the push–push operation, it should be verified that the resonance with the capacitance range of the process affordable varactor and L_{branch} occurs at f_{push}, while the Q-factor of the branch (Q_{branch}) is higher than $Q_{\min}$.

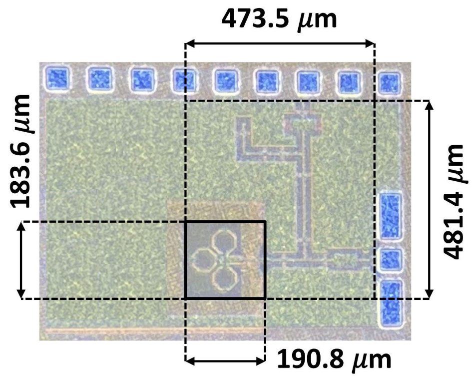

Fig. 14. Chip micrograph of the proposed dual-band VCO.

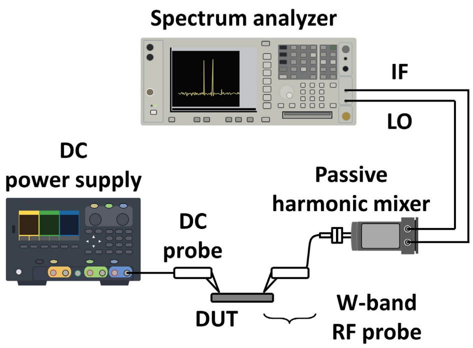

Fig. 15. Measurement setup for the *W*-band VCO performance validation.

The oscillation core is used to provide a negative G_m; therefore, the simulation should be based on the post-layout results of the clover-shaped inductor. The target oscillation frequencies should be tested by adjusting the transistor size and bias, while ensuring that the varactor provides a sufficient FTR. The reconfigurable push operation is verified by fabricating a VCO designed based on the final obtained parameters.

IV. Measurement Results

As a proof of concept, the proposed VCO was fabricated with a Samsung 28-nm CMOS process with an active core size of 0.19 × 0.18 mm. A micrograph of the fabricated chip is shown in Fig. 14. The power supply used in the chip was from a PGP dc probe with a bias tee network in the VCO. Both second- and third-harmonic signals were measured at the output port using the same test setups, as shown in Fig. 15. The losses of the cables and waveguide connectors were calibrated using a Keysight W8486 power sensor. The oscillation frequency and phase noise were measured using a Keysight E4448 spectrum analyzer with a Keysight 11970W *W*-band harmonic mixer.

Fig. 16(a) and (b) demonstrates the FTR and output power as measured through a varactor control process with a 1.4-V supply voltage, consuming 21.21 and 62.23 mW for the push–push and triple-push operations, respectively. The triple-/push–push operation for band shifting is determined by the core ON/OFF state. With a change in the control voltage, the measured tuning ranges for push–push and triple-push operations are 86.29–95.79 and 95.1–109.55 GHz, respectively. The tuning voltage for all the varactors was set to the same

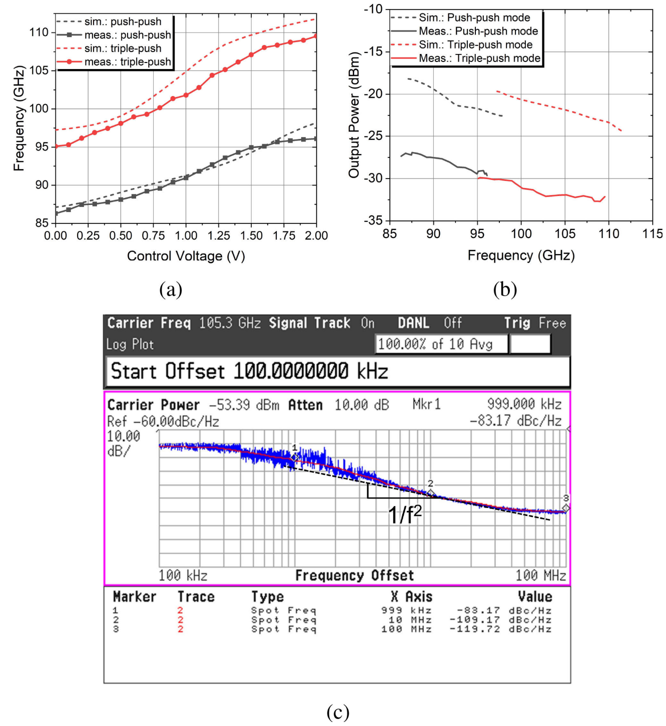

Fig. 16. Measured/simulated (a) FTR, (b) output power of the dual-band VCO, and (c) phase noise measurement result.

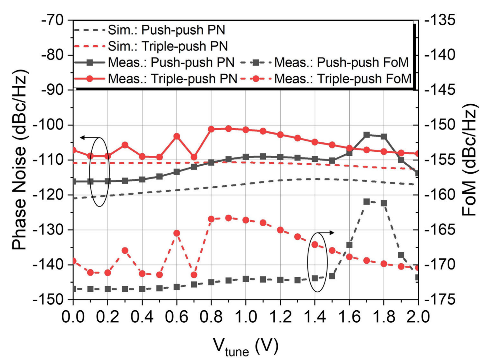

Fig. 17. Simulated and measured phase noise, and FoM for the varactor control voltage range.

value and changed simultaneously. The frequency overlap between two bands was designed while considering the frequency shift due to the error caused by the process and temperature. The proposed dual-band VCO achieves a band overlap of 690 MHz by employing a control voltage in the range of 0–2 V. Fig. 16(c) illustrates the phase noise measured at 105.3 GHz when operating in the triple-push mode. The phase noise outcomes at 1- and 10-MHz offsets are correspondingly −83.17 and −109.17 dBc/Hz, respectively. In addition, the simulated and measured phase noise and FoM with respect to the varactor tuning voltage are plotted in Fig. 17. The measured average FoM is −168 and −171.1 dBc/Hz for triple-push and push–push mode operation, respectively. The lowest FoM for each motion is −171.4 and −173.5 dBc/Hz, respectively.

The performance of the proposed VCO is compared with prior state-of-the-art single-band and dual-band VCOs whose data are presented in Tables I and II, respectively. The FoM

TABLE I
PERFORMANCE COMPARISON WITH THE STATE-OF-THE-ART SUB-THZ SINGLE-BAND VCOS

References	Tech.	Topology	Freq. (GHz)	FTR (%)	PN@1MHz (dBc/Hz)	PN@10MHz (dBc/Hz)	P_{DC} mW	FoM (dBc/Hz)	FoM_T (dBc/Hz)	Area (mm^2)
[19] TMTT'14	0.13-μm CMOS	Fundamental	96.5	8.3	-102	-124.5	90	-190.3 ~ -178*	-188.7 ~ -176.5*	0.048
[20] MWCL'15	90-nm CMOS	Tripling	82.65	15.61	-87.9	NA	62.4	-168.3 ~ -156.2	-172.2 ~ -160.1	1.3
[5] TMTT'15	65-nm CMOS	Push-push	163	14	-91.3	NA	33	-179.7 ~ -172.5*	-182.6 ~ -175*	0.046
[21] TMTT'15	65-nm CMOS	Push-push	102.7	11.4	-88	NA	36	-176.7 ~ -172.7	-177.9 ~ -173.9	0.068
[7] RFIT'16	90-nm CMOS	Push-push	114.5	4.4	-93	NA	36	-178.4**	-171.5**	0.033
[10] TMTT'18	90-nm CMOS	Triple-push	210	5.1	-88	-111.5	28.6	-183.4 ~ -163*	-174 ~ -157.4*	0.17
[22] RFIC'19	65-nm CMOS	Fundamental	89.3	8.3	-91.8	NA	8.5	-181.5**	-179.8**	0.25
[6] RFIT'21	90-nm CMOS	Push-push	90.1	2.24	-83.52	-109.22	25.43	-174.3 ~ -164*	-161.3 ~ -151*	0.31
This Work	28-nm CMOS	Push-push Triple-push	91 102.3	10.4 14.1	-87.56 -83.17	-115.9 -109.17	21.21 62.21	-173.5 ~ -161 -171.4 ~ -163.3	-173.9 ~ -161.4 -174.4 ~ -166.3	0.035

* : The value estimated from the result graph. ** : Only the best case is provided.

TABLE II
PERFORMANCE COMPARISON WITH THE STATE-OF-THE-ART SUB-THZ DUAL-BAND VCOS

References	Tech.	Topology	Freq. (GHz)	FTR (%)	PN@1MHz (dBc/Hz)	PN@10MHz (dBc/Hz)	P_{DC} mW	FoM (dBc/Hz)	FoM_T (dBc/Hz)	Area (mm^2)
[23] ISIC'14	65-nm CMOS	Fundamental dual-band	76.8 79.25	1.04 1.89	-90.8	-113.3	30	-176.6	-162.1	0.032
[24] RFIC'15	28-nm CMOS	Fundamental QVCO	73.75 88.15	6.37 5.79	-93.5 -86.2	-117.7 -110	35.6	-179.4 -173.4	-175.6 -168.6	0.031
[25] TMTT'16	65-nm CMOS	Inductive dividing	75.9 89.4	7.38 5.15	-85.3 -81.5	-109.4 -108.3	12 11	-176.2 -176.9	-173.6 -171.1	0.013
[13] IMS'19	90-nm CMOS	Standing-wave dual-band	21.5 74.5	8.4 1.3	-103.2 -91.2	NA NA	7.2 16.8	-180.1 -176.4	-179.7 -158.9	0.088
This Work	28-nm CMOS	Switch-less reconfigurable-push	97.92	23.75	-83.17	-109.17	21.21 62.21	-171.1	-178.6	0.035

and FoM_T are evaluated as follows:

$$\mathrm{FoM} = L(\Delta f) - 20\log(f_{\mathrm{osc}}/\Delta f) + 10\log(P_{\mathrm{dc}}/1\ \mathrm{mW}) \tag{11}$$

$$\mathrm{FoM}_T = \mathrm{FoM} - 20\log(10\cdot \mathrm{FTR}). \tag{12}$$

When considering the die area consumption, the implementation of the proposed topology demonstrated a comparable or better FoM_T performance compared with the sub-THz single-band VCOs. Upon comparison with the dual-band characteristics, the proposed VCO achieved an overlap between the two oscillation bands, leading to a wide FTR. Considering the comparison with VCOs from previous dual-band studies, the proposed VCO achieved a superb FoM_T performance with a wide FTR through the overlap between the two bands.

V. CONCLUSION

A reconfigurable push VCO with a switchless dual-band operation in the W-band was designed based on the proposed clover-shaped inductor, which has a symmetrical layout to enable the implementation of the push–push or triple-push reconfiguration. The VCO design consists of three cores providing negative transconductances, combined with the proposed clover-shaped inductor, which forms a structure with three ports for core connection and a multiplied frequency output port. A structure with three directly connected oscillation cores based on a cross-coupled structure makes it possible to achieve a phase difference of 120° and 180° by the vector sum. The proposed topology enables reconfigurable oscillation-band control without loading switches in the RF path. The measured dual-band VCO achieved an FoM_T value of −178.6 dBc/Hz occupying an area of 0.035 mm^2.

ACKNOWLEDGMENT

The chip fabrication and EDA tool were supported by the IC Design Education Center (IDEC), South Korea.

References

[1] W. Saad, M. Bennis, and M. Chen, "A vision of 6G wireless systems: Applications, trends, technologies, and open research problems," *IEEE Netw.*, vol. 34, no. 3, pp. 134–142, May/Jun. 2020.

[2] H.-Y. Chang, H. Wang, M. Yu, and Y. Shu, "A 77-GHz MMIC power amplifier for automotive radar applications," *IEEE Microw. Wireless Compon. Lett.*, vol. 13, no. 4, pp. 143–145, Apr. 2003.

[3] S. Hu, C. Shu, Y. Alfadhl, and X. Chen, "W band imaging system using linear sparse periodic antenna array and compressive sensing for personnel screening," *IEEE Access*, vol. 7, pp. 173603–173611, 2019.

[4] A. Kurdoghlian et al., "First demonstration of broadband W-band and D-band GaN MMICs for next generation communication systems," in *IEEE MTT-S Int. Microw. Symp. Dig.*, Honolulu, HI, USA, Jun. 2017, pp. 1126–1128.

[5] H. Koo, C.-Y. Kim, and S. Hong, "A G-band standing-wave push–push VCO using a transmission-line resonator," *IEEE Trans. Microw. Theory Techn.*, vol. 63, no. 3, pp. 1036–1045, Mar. 2015.

[6] S.-H. Liu, C.-M. Hung, H.-R. Chuang, and T.-H. Huang, "A W-band push-push VCO with gm-boosted Colpitts topology in 90-nm CMOS technology," in *Proc. IEEE Int. Symp. Radio-Frequency Integr. Technol. (RFIT)*, Aug. 2021, pp. 1–3.

[7] C.-Y. Yang, S.-Y. Li, S. C.-L. Hsieh, and J. Y.-C. Liu, "A push-push voltage-controlled oscillator for W-band applications in 90-nm CMOS," in *Proc. IEEE Int. Symp. Radio-Freq. Integr. Technol. (RFIT)*, Aug. 2016, pp. 1–3.

[8] C.-C. Chen, C.-C. Li, B.-J. Huang, K.-Y. Lin, H.-W. Tsao, and H. Wang, "Ring-based triple-push VCOs with wide continuous tuning ranges," *IEEE Trans. Microw. Theory Tech.*, vol. 57, no. 9, pp. 2173–2183, Sep. 2009.

[9] B. Catli and M. M. Hella, "Triple-push operation for combined oscillation/divison functionality in millimeter-wave frequency synthesizers," *IEEE J. Solid-State Circuits*, vol. 45, no. 8, pp. 1575–1589, Aug. 2010.

[10] C.-L. S. Hsieh and J. Y.-C. Liu, "A low phase noise 210-GHz triple-push ring oscillator in 90-nm CMOS," *IEEE Trans. Microw. Theory Techn.*, vol. 66, no. 4, pp. 1983–1997, Apr. 2018.

[11] I. Mansour, M. Aboualalaa, A. Allam, A. B. Abdel-Rahman, M. Abo-Zahhad, and R. K. Pokharel, "Dual band VCO based on a high-quality factor switched interdigital resonator for the Ku band using 180-nm CMOS technology," *IEEE Trans. Circuits Syst. II, Exp. Briefs*, vol. 65, no. 12, pp. 1874–1878, Dec. 2018.

[12] J. Baylon, P. Agarwal, L. Renaud, S. N. Ali, and D. Heo, "A Ka-band dual-band digitally controlled oscillator with -195.1-dBc/Hz FoM_T based on a compact high-Q dual-path phase-switched inductor," *IEEE Trans. Microw. Theory Tech.*, vol. 67, no. 7, pp. 2748–2758, Jul. 2019.

[13] C.-M. Lin, Y.-T. Lin, K.-Y. Kao, and K.-Y. Lin, "A dual-band CMOS standing-wave digitally controlled oscillator for automotive radars," in *IEEE MTT-S Int. Microw. Symp. Dig.*, Jun. 2019, pp. 385–388.

[14] S. Oh, J. Kim, and J. Oh, "Sub- THz switch-less reconfigurable triple-/push-push dual-band VCO for 6G communication," in *Proc. IEEE Radio Freq. Integr. Circuits Symp. (RFIC)*, Jun. 2022, pp. 219–222.

[15] A. Collado and A. Georgiadis, "Nonlinear mode analysis and optimization of a triple-push oscillator," *IEEE Microw. Wireless Compon. Lett.*, vol. 18, no. 8, pp. 545–547, Aug. 2008.

[16] D. E. Bockelman and W. R. Eisenstadt, "Pure-mode network analyzer for on-wafer measurements of mixed-mode S-parameters of differential circuits," *IEEE Trans. Microw. Theory Techn.*, vol. 45, no. 7, pp. 1071–1077, Jul. 1997.

[17] X. Xu, W. Zou, J. Du, X. Chen, and X. Zou, "Predictive calculation of coupling coefficient between on-chip small-area multilayer inductors," in *Proc. IEEE 11th Int. Conf. Solid-State Integr. Circuit Technol.*, Oct. 2012, pp. 1–4.

[18] R. Bostani, G. Ardeshir, and H. Miar-Naimi, "Analysis of millimeter-wave LC oscillators based on two-port network theory," *IEEE Trans. Circuits Syst. II, Exp. Briefs*, vol. 64, no. 3, pp. 239–243, Mar. 2017.

[19] S. Kang, J. C. Chien, and A. M. Niknejad, "A W-band low-noise PLL with a fundamental VCO in SiGe for millimeter-wave applications," *IEEE Trans. Microw. Theory Techn.*, vol. 62, no. 10, pp. 2390–2404, Oct. 2014.

[20] K.-W. Tan, T.-S. Chu, and S. S. H. Hsu, "A 76.2–89.1 GHz phase-locked loop with 15.6% tuning range in 90 nm CMOS for W-Band applications," *IEEE Microw. Wireless Compon. Lett.*, vol. 25, no. 8, pp. 538–540, Aug. 2015.

[21] Y. Chao, H. C. Luong, and Z. Hong, "Analysis and design of a 14.1-mW 50/100-GHz transformer-based PLL with embedded phase shifter in 65-nm CMOS," *IEEE Trans. Microw. Theory Tech.*, vol. 63, no. 4, pp. 1193–1201, Apr. 2015.

[22] A. Tarkeshdouz, M. H. Kashani, E. H. Hafshejani, S. Mirabbasi, and E. Afshari, "An 82.2-to-89.3 GHz CMOS VCO with DC-to-RF efficiency of 14.8%," in *Proc. IEEE Radio Freq. Integr. Circuits Symp. (RFIC)*, Jun. 2019, pp. 331–334.

[23] J. Lee, Y. Moon, and T. Ahn, "A dual-band VCO using inductor splitting for automotive radar system at W-band," in *Proc. Int. Symp. Integr. Circuits (ISIC)*, Dec. 2014, pp. 168–171.

[24] M. Vigilante and P. Reynaert, "A dual-band E-band quadrature VCO with switched coupled transformers in 28 nm HPM bulk CMOS," in *Proc. IEEE Radio Freq. Integr. Circuits Symp. (RFIC)*, May 2015, pp. 119–122.

[25] T. Xi, S. Guo, P. Gui, D. Huang, Y. Fan, and M. Morgan, "Low-phase-noise 54-GHz transformer-coupled quadrature VCO and 76-/90-GHz VCOs in 65-nm CMOS," *IEEE Trans. Microw. Theory Techn.*, vol. 64, no. 7, pp. 2091–2103, Jul. 2016.

Seongwoog Oh (Graduate Student Member, IEEE) received the B.S. degree in electrical engineering and computer science from the Gwangju Institute of Science and Technology College, Gwangju, South Korea, in 2016, and the M.S. degree in electrical engineering from Seoul National University, Seoul, South Korea, in 2018, where he is currently pursuing the Ph.D. degree in electrical engineering.

His current research interests concerned the design of microwave integrated circuits, antenna-on-package systems for 5G/6G communication, and microwave brain stimulation.

Jinhyun Kim (Graduate Student Member, IEEE) received the B.S. degree in electrical engineering from Hanyang University, Ansan, South Korea, in 2019. He is currently pursuing the M.S. degree at Seoul National University, Seoul, South Korea.

His current research interests concerned the design of microwave integrated circuits and systems for 5G communication and brain stimulation.

Jungsuek Oh (Senior Member, IEEE) received the B.S. and M.S. degrees from Seoul National University, Seoul, South Korea, in 2002 and 2007, respectively, and the Ph.D. degree from the University of Michigan, Ann Arbor, MI, USA, in 2012.

From 2007 to 2008, he was with Korea Telecom as a Hardware Research Engineer, working on the development of flexible RF devices. In 2012, he was a Post-Doctoral Research Fellow with the Radiation Laboratory, University of Michigan. From 2013 to 2014, he was a Staff RF Engineer with Samsung Research America, Dallas, TX, USA, working as a Project Leader for the 5G/millimeter-wave antenna system. From 2015 to 2018, he was a Faculty Member with the Department of Electronic Engineering, Inha University, Incheon, South Korea. He is currently an Associate Professor with the School of Electrical and Computer Engineering, Seoul National University. He has published more than 50 technical papers. His research areas include mmWave/THz beam focusing/shaping techniques, antenna miniaturization for integrated systems, and radio propagation modeling for indoor scenarios.

Dr. Oh was a recipient of the 2011 Rackham Predoctoral Fellowship Award at the University of Michigan, the 2018 SNU Creative-Pioneering Research Award, and the 2019 IEEE AP-S/MTT Seoul Chapter Best Paper Award. He has been an Associate Editor for *Microwave and Optical Technology Letters* and *ICT Express*. He has served as a TPC member and as a session chair for the IEEE Antennas and Propagation Society (AP-S) and the US National Committee (USNC) of the International Union of Radio Science (URSI), the International Symposium on Antennas and Propagation (ISAP).